RESEARCH ARTICLE

ADVANCED FUNCTIONAL MATERIALS
www.afm-journal.de

Ultra-Fast Pulsed Discharge Preparation of Coordinatively Unsaturated Asymmetric Copper Single-Atom Catalysts for CO_2 Reduction

Kaiyuan Liu, Zhiyi Sun, Wenxing Chen, Xiufeng Lang, Xin Gao,* and Pengwan Chen**

Single-atom catalysts possess great potential for applications in electrochemical carbon dioxide reduction reactions. Recently, the fast and low-cost preparation of highly efficient single-atom catalysts remains a challenge. Herein, a high-density current generated by pulsed discharge is employed for the formation of graphene aerogel anchored Cu single atom catalysts perfectly. The Cu atoms decomposed by $Cu(NO_3)_2{\bullet}xH_2O$ are fixed on graphene under the local transient high temperature and intense electromagnetic field. The activity and selectivity of formic acid are correlated with the coordinatively unsaturated $Cu{-}N_1O_1$ moieties, reaching an optimal Faradaic efficiency (93.7%) at −0.9 V versus a reversible hydrogen electrode (RHE). In situ characterizations reveal that the asymmetric Cu—N/O structure in a pinched state displays better catalytic activity in CO_2RR. Density functional theory results indicate that the $Cu{-}N_1O_1$ sites regulate the adsorption configuration of intermediates and lower the energy barrier for the hydrogenation of *OCHO species, thereby promoting CO_2-to-HCOOH conversion.

1. Introduction

The electrochemical carbon dioxide reduction reaction (CO_2RR) using renewable electricity provides an attractive way to produce environmentally friendly hydrocarbon fuels or chemicals, offsetting additional greenhouse gas emissions.[1–3] Formic acid (HCOOH) production by CO_2RR technology is a very economical strategy, which has the advantages of a simple reaction path, low energy barrier, and a small number of electrons (only two electrons) involved in the reaction transfer.[4,5] In recent years, some metallic elements such as tin (Sn), bismuth (Bi), indium (In), lead (Pb), and palladium (Pd) have been reported as electrochemical catalysts for HCOOH production from CO_2.[6–13] However, the low Faraday efficiency and high overpotential increase the production costs and limit the practical applications.[14,15] Copper (Cu) is considered one of the most promising electrocatalysts for CO_2RR because of its high activity and low cost, especially, formic acid can be highly selectively produced by a properly designed Cu atomic interface as well.[16–19]

Single-atom catalysts (SACs), consisting of single metal atoms and adjacent coordination species in an atomic level dispersion state, constitute an active catalytic group, which not only provide almost 100% atom utilization efficiency but also have an adjustable electronic structure.[20–23] SACs perform great potential in electrochemically catalyzing the synthesis of formic acid from CO_2RR, due to the unique isolated atomic interfaces.[24–27] Therefore, understanding the relationship between atomic interface and performance could further guide the rational design of novel, high-performance SACs for the CO_2RR process.[11,28–29] Moreover, the novel synthesis strategy and delicate control of experimental conditions are also significant to the atomic interface adjustment of SACs. The ultrafast pyrolysis strategy with the rapid high-temperature input and high cooling rate, provides great opportunities for the preparation of new-type SACs in a cost-effective manner.[30–32] As a member of rapid synthesis, a period of current pulse induced by high voltage can be used to prepare stable SACs through instantaneous Joule heating and ultrafast cooling rate.[33]

The controlled pulsed power can be applied to induce the local atom reconstruction to form SACs. With respect to the pulsed discharge method, it features an intense electromagnetic field and the current pulse with a period of 10^2–10^3 μs and a peak value of 10^5 A.[34] Thus, pulsed power can completely

---

K. Liu, X. Gao, P. Chen
School of Mechatronical Engineering
Beijing Institute of Technology
Beijing 100081, China
E-mail: gaoxin@bit.edu.cn; pwchen@bit.edu.cn

Z. Sun, W. Chen
Energy & Catalysis Center
School of Materials Science and Engineering
Beijing Institute of Technology
Beijing 100081, China

X. Lang
Department of Physics
Hebei Normal University of Science & Technology
Qinhuangdao 066004, China
E-mail: langxf811015@126.com

P. Chen
School of Materials and Engineering
Beijing Institute of Technology
Beijing 100081, China

The ORCID identification number(s) for the author(s) of this article can be found under https://doi.org/10.1002/adfm.202312589

DOI: 10.1002/adfm.202312589

sublimate the precursor to form a mixture of separated single atoms and ions under proper conditions. After the discharge, the products cool down rapidly to form nanoparticles including quantum dots. In recent reports, with proper substrate materials and delicate control of energy input, certain nanomaterials with specific structures can be obtained on the substrate materials, for example, nanoparticles, nanoclusters, and even SACs.[35–38] These researches indicate that certain atomic structures can be achieved using proper matrix material with proper discharge conditions. Thus, we believe that it is also feasible to prepare a novel coordinatively unsaturated asymmetric SAC through ultrafast pulsed discharge investigation.

In this work, a unique graphene aerogel supported Cu single atom catalyst (CuN_1O_1 SAs/GAs) is synthesized rapidly by a pulsed discharge route. The resulting extreme thermal shock and intense electromagnetic field induce in situ nitrogen doping of graphene aerogels, meanwhile achieving atomic dispersion of Cu species. Moreover, the asymmetric $Cu—N_1O_1$ coordination moiety is validated by structural analysis at the atomic level. Impressively, the CuN_1O_1 SAs/GAs exhibit excellent selectivity and activity at a wide potential range in CO_2RR to produce formic acid, and this catalyst performs excellent stability (> 10 h) over 90% Faradaic efficiency (FE) with a stable current density (-19 mA cm^{-2}). In situ X-ray absorption fine structure (XAFS) tests for CuN_1O_1 SAs/GAs reveal that the stretch Cu—N/O bonds would promote HCOOH production from CO_2RR. Finally, the first-principle calculations manifest that the energy barrier of formic acid is lower than CO, and HCOOH is more likely to be produced on the coordinatively unsaturated $Cu—N_1O_1$ moieties. Different metal SACs with the local structure of $M—N_1O_1$ (M = Mn, Fe, Co, and Ni) can also be synthesized through pulsed discharge processes with different precursors.

2. Results and Discussion

2.1. Synthesis and Morphology Characterizations of CuN_1O_1 SAs/GAs

Graphene hydrogel was assembled by hydrothermal reduction method, and then graphene aerogels (GAs, Figures S1 and S2, Supporting Information) could be obtained after freeze-drying. When copper nitrate ($Cu(NO_3)_2$) with the loading of 10 wt.% was fully dissolved in graphene hydrogel, graphene aerogel loaded copper nitrate ($Cu(NO_3)_2{\bullet}xH_2O$/GA) would be prepared after the same freeze-drying process. The $Cu(NO_3)_2{\bullet}xH_2O$/GA was filled into the discharge tube and connected to the pulsed discharge circuit (Figures S3 and S4, Supporting Information). After charging the capacitor bank (250 μF, 8 kV), the discharge was triggered to generate an intense current pulse. Then, $Cu(NO_3)_2$ was decomposed into Cu and nitrogen oxides (N_xO_y) in the cavity under the action of rapid Joule heat. Nitrogen (N) atoms from the N_xO_y were doped into the reduced graphene oxide (rGO) structure with defects. Meanwhile, the pulsed discharge would also promote oxygen activation in the air to combine with rGO. The decomposed Cu from $Cu(NO_3)_2$ sublimated due to high temperature, and anchored onto rGO in the form of single Cu atoms. After eight repeated pulsed discharges, the graphene aerogel was uniformly loaded with Cu atoms (CuN_1O_1 SAs/GA), the formation schematic diagram of CuN_1O_1 SAs/GA is shown in **Figure 1a**.

The presentative discharge current and voltage waveforms are shown in Figure S5 (Supporting Information), revealing the typical underdamping-type *I–U* (current and voltage) waveforms in pulsed discharge circuit. Particularly, the *I-U* waveforms of $Cu(NO_3)_2{\bullet}xH_2O$/GA filling in the discharged tube (Figure S5b, Supporting Information) demonstrate that the resistance of the discharge circuit has no change during pulsed discharge. It indicates that the GA support features no phase change and decomposition under such pulsed discharge action, as evidenced by the recovered intact sample after discharge treatment. Moreover, the peak values and duration of *I–U* waveforms (Table S1, Supporting Information) reveal the presence of current passing through $Cu(NO_3)_2{\bullet}xH_2O$/GA. The intense current induces the transient high-temperature of GA and a strong electromagnetic field. Therefore, the $Cu(NO_3)_2{\bullet}xH_2O$ nanocrystals in GA decomposed to form Cu^{2+} ions and *NO ions burst out in GA. Under the action of the intense electric field between two electrodes, these ions were forced to move and separate on the graphene layer surface during pulsed discharge. Furthermore, the air gaps between GAs and copper plugs break down to form arc discharge channels during the pulsed discharge process, also generating N ions and O ions.[39] In addition, the air in the porous structure of GAs might form corona discharge plasma under the actions of ions from $Cu(NO_3)_2{\bullet}xH_2O$ nanocrystals and the intense electric field. The radial expansion of above formed ions is inhibited by the magnetic pinch effect during pulsed discharge.[40] When the discharge current decreases in microseconds, the activity of Cu, N, and O ions decreases and the plasma can hardly be maintained. Consequently, the Cu, N, and O atoms are anchored and fixed in the defects in the graphitic layers to form certain stable structures such as CuN_1O_1 single atom anchoring structure (Figure S6, Supporting Information). Of course partial ion mixtures from $Cu(NO_3)_2{\bullet}xH_2O$ might be from Cu clusters and CuO nanocrystals that could be purified after the repeated pulsed discharge processes.

The morphology characterizations of discharged CuN_1O_1 SAs/GAs are displayed in Figure 1b–g. Figure 1b shows the scanning electron microscope (SEM) image of CuN_1O_1 SAs/GAs, the basic structure of 3D porous aerogel is still intact, this feature has not been destroyed by repeated discharge. The 3D crimped graphene structure can be clearly identified in the transmission electron microscope (TEM) image (Figure 1c). The X-ray diffraction (XRD) results of CuN_1O_1 SAs/GAs only showed the characteristic peaks of rGO (Figure S7, Supporting Information), indicating that no Cu nanoparticles remained on the surface of GAs. Carbon (C), oxygen (O), nitrogen (N), and Cu were uniformly dispersed on graphene in the local TEM mapping of GAs (Figure 1d; Figure S8, Supporting Information). Therefore, it is reasonable to speculate that N and Cu are doped into GAs in the process of pulsed discharge. To confirm the dispersion of Cu atoms on the support, Figure 1e illustrates a high-angle annular dark-field scanning transmission electron microscopy (HAADF-STEM) picture of CuN_1O_1 SAs/GAs. A lot of isolated bright spots are evenly dispersed on the rGO surface. In addition, by comparing the characterization results (SEM, TEM, XRD) of GA support before and after pulse discharge, it can be confirmed that they have no phase transition or decomposition. Figure 1f is a partially

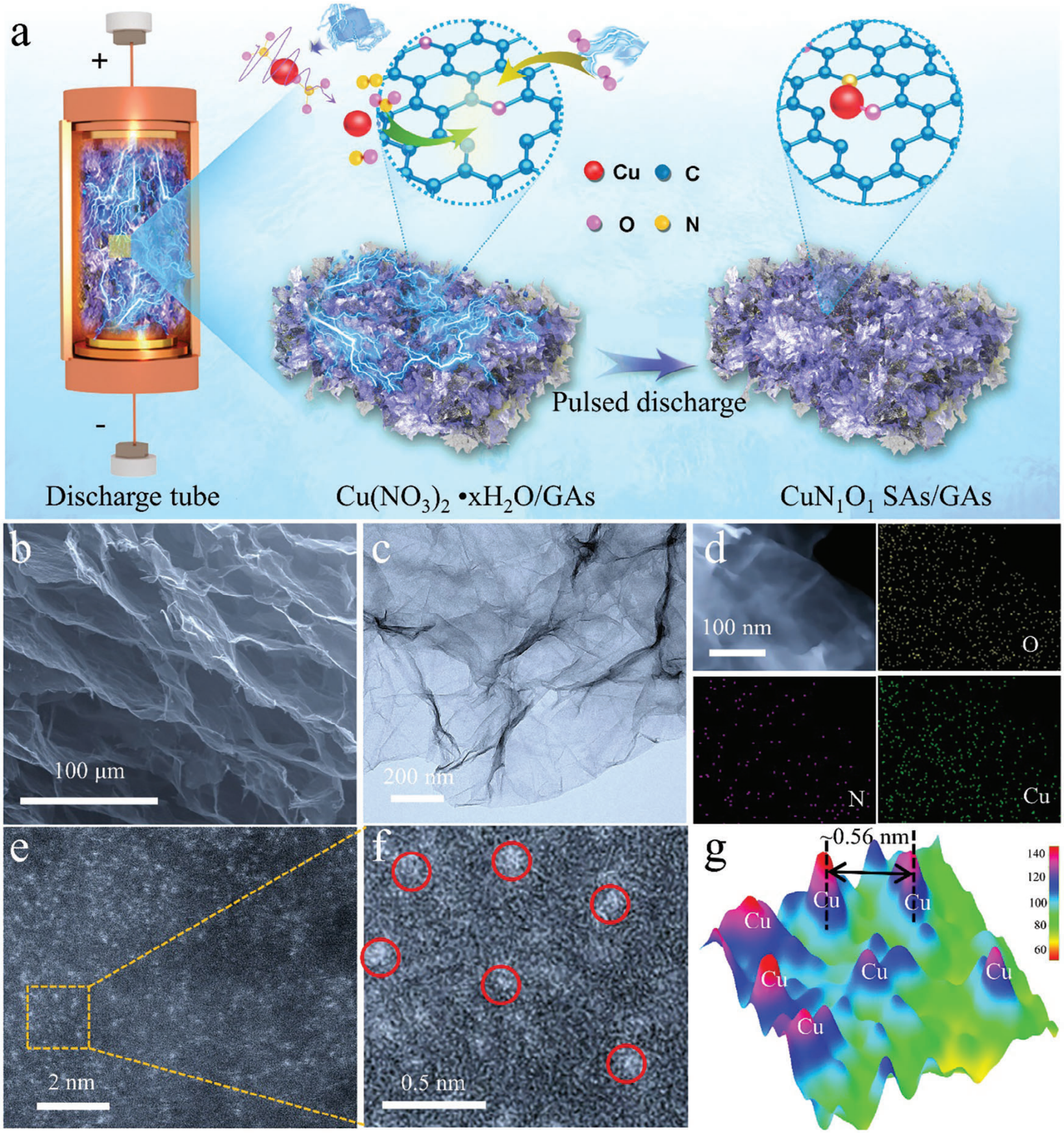

Figure 1. The synthesis and characterizations of CuN_1O_1 SAs/GAs: a) The schematic diagram of preparation strategy by pulsed discharge. b) SEM, c) TEM and d) EDS images of CuN_1O_1 SAs/GAs, C (green), O (purple), and Cu (red). e) HAADF-STEM image and f) the magnified image of CuN_1O_1 SAs/GAs. g) The corresponding intensity profiles for (f).

enlarged view of Figure 1e, and the Cu atoms are marked by red circles. In order to more clearly distinguish between Cu atoms and rGO, Figure 1g shows the 3D color distribution of CuN_1O_1 SAs/GAs, corresponding to Figure 1f. The red bulges are considered to be Cu atoms, the green distribution is rGO, and the typical distance between two Cu atoms is ≈0.56 nm. The EDS mapping results showed a Cu content of ≈1.03 at% (Figure S9, Supporting Information). Interestingly, when $CuCl_2$ was used as a precursor to provide Cu atoms, Cu atoms formed Cu nanoparticles loaded onto rGO (Cu NPs/GAs) through pulsed discharge treatment (Figure S10, Supporting Information), suggesting the important role of the nitrate on anchoring and stabilizing isolate Cu atoms. In addition, we synthesized CuN_4 SAs/GAs (Cu atoms were coordinated with four nitrogen atoms) as a comparative sample in this study (Note S1, Supporting Information).

2.2. Chemical State and Atomic Structure Analysis of CuN_1O_1 SAs/GAs

XAFS based on a synchrotron radiation accelerator was used to detect the interaction of electrons and atoms of Cu, O, N, and C in CuN_1O_1 SAs/GAs. **Figure 2a** shows the K-edge absorption curves of GO, CuN_1O_1 SAs/GAs, and defect-free graphene under soft X-ray. Three typical peaks at different photon energy positions correspond to different types of chemical bonds. Generally, it is

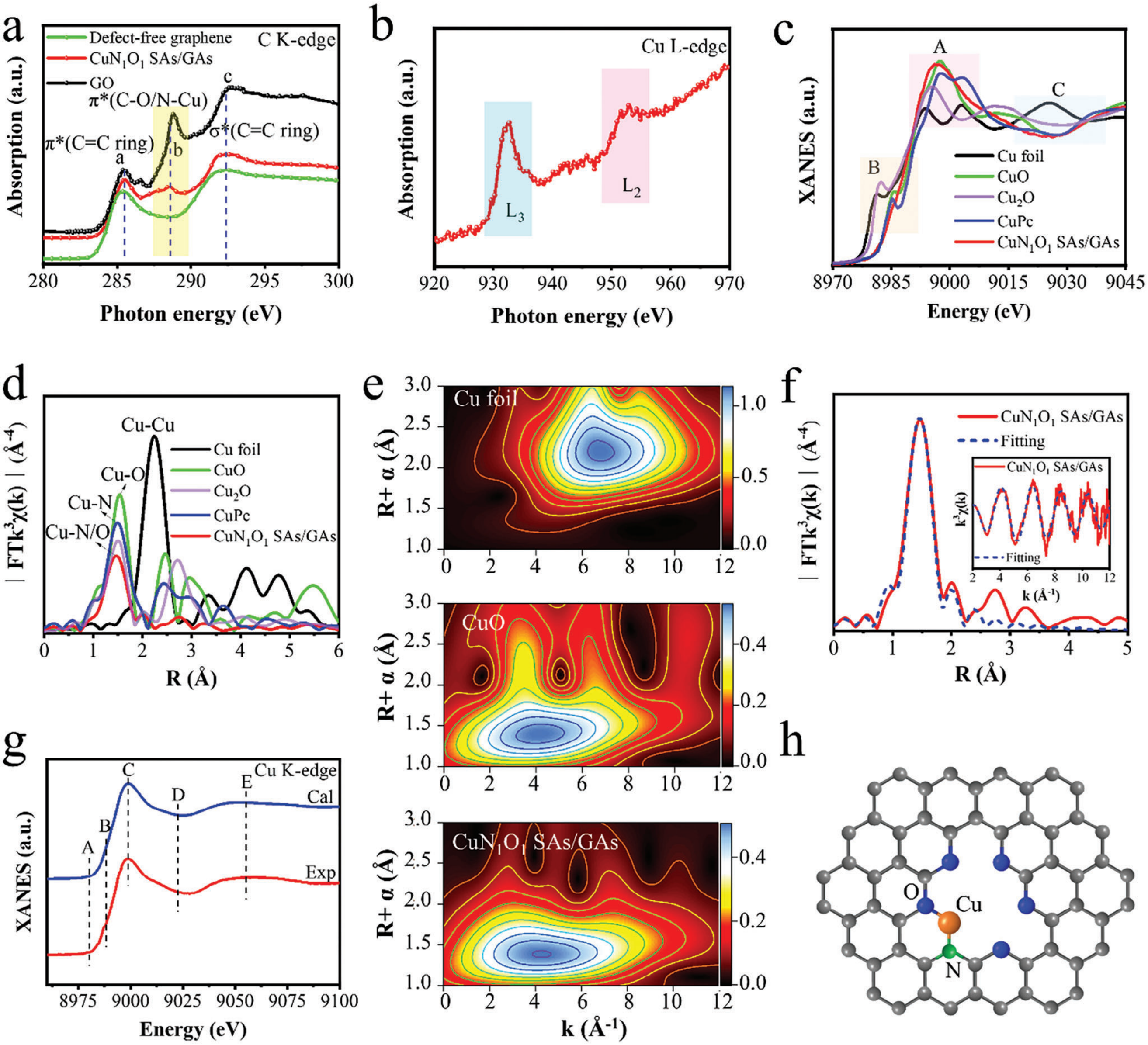

Figure 2. Chemical state and atomic coordination structure of CuN_1O_1 SAs/GAs. a) C K-edge XANES spectra of GAs and no defects graphene. b) Cu L-edge and c) The experimental Cu K-edge XANES spectra of CuN_1O_1 SAs/GAs and the references (Cu foil, CuO, Cu_2O, CuPc). d) FT k^3-weighted Cu K-edge EXAFS spectra of CuN_1O_1 SAs/GAs and the references. e) WT-EXAFS plots of CuN_1O_1 SAs/GAs, Cu foil and CuO, respectively. f) FT-EXAFS fitting curve of CuN_1O_1 SAs/GAs at the Cu K-edge, the inset is the EXAFS fitting curve of CuN_1O_1 SAs/GAs in k space. g) The path of Cu K-edge experiment and calculation. h) Schematic atomic structure model of CuN_1O_1 SAs/GAs.

believed that the type of C═C ring is π^* and σ^* at 285.5 and 292.5 eV, respectively.[41] As the most oxygen-containing group, GO shows the most obvious peak at 288.5 eV. In contrast, a smooth and no peak curve of defect-free graphene appears at the same position. When the oxygen-containing group is partially removed by reduction and loaded with Cu single atoms (CuN_1O_1 SAs/GAs), the K-edge of C displays a weak peak at 288.8 eV, which is lower than the peak of the pristine GO at region b. The Cu L-edge XAFS spectra of CuN_1O_1 SAs/GAs are shown in Figure 2b. The near edge absorption energy has two definite peak positions, L_3 and L_2 edges at 932.6 and 952.9 eV, respectively, coinciding with Cu^{2+}.[42] The K-edge XAFS results (Figure S11, Supporting Information) of N and O demonstrate the co-doping of N and O on rGO, which is consistent with the results of X-ray photoelectron spectroscopy (XPS), as shown in Figure S12 (Supporting Information). After pulsed discharge treatment, the content of oxygen atoms, defects, and the number of nanopores in rGO were increased obviously (Figures S13–S15, Supporting Information).

The Cu K-edge X-ray absorption near-edge structure (XANES) results of CuN_1O_1 SAs/GAs and references are shown in Figure 2c and Figure S16a (Supporting Information). The region

A of CuN_1O_1 SAs/GAs originates from the transition from 1s to $4p_z$. The absorption edge of CuN_1O_1 SAs/GAs (region B) is closer to that of CuO, but far away from Cu_2O and Cu foil, which implies that the valence state of Cu in CuN_1O_1 SAs/GAs is about Cu^{2+}. Moreover, CuN_1O_1 SAs/GAs showed a flatter trend in the post-edge feature C, which was different from CuO, Cu_2O, and Cu foil. The Fourier transform (FT) k^3-weighted extended X-ray absorption fine structure (EXAFS) spectra of CuN_1O_1 SAs/GAs and references were illustrated in Figure 2d and Figures S16–S18 (Supporting Information). The typical FT peak of CuN_1O_1 SAs/GAs was located at 1.47 Å, which was between the peaks of Cu—O path and Cu—N path (Figure S19, Supporting Information), it was presumed that the Cu atom is co-coordinated with N and O in CuN_1O_1 SAs/GAs.[43,44] In addition, it is not found the peak of Cu—Cu coordination in CuN_1O_1 SAs/GAs, compared with the results of Cu foil.

Based on the high resolution in R and k space, the powerful Cu K-edge wavelet transform (WT) EXAFS was used to discriminate backscattered atoms,[45] and the results of CuN_1O_1 SAs/GAs and references were shown in Figure 2e. The WT-EXAFS contour plot of CuN_1O_1 SAs/GAs exhibited one intensity maximum (4.3 $Å^{-1}$). Compared with the first-shell intensity maximum of CuO (4.1 $Å^{-1}$) and CuN_4 SAs/GAs (4.4 $Å^{-1}$), this further demonstrated that the coordinate structure of Cu in the first shell is Cu—O/Cu—N. In addition, the absence of a Cu—Cu bond (Cu foil: 6.8 $Å^{-1}$) in the contour plots of CuN_1O_1 SAs/GAs, so the distribution of atomically dispersed Cu atoms on graphene was fully confirmed. The structural parameters of Cu K-edge could be quantitatively obtained by the least-square EXAFS fitting (Figure 2f; Figure S17 and Table S2, Supporting Information). As we can see, the fitting and experimental curves of CuN_1O_1 SAs/GAs are matched well in the R, k, and q space. Based on the fittings, the coordination number in the first shell of Cu was estimated to be two (one nitrogen atom and one oxygen atom). Furthermore, the calculated XANES spectrum based on the atomic structure of Cu—N_1O_1 was also compared with the experimental one (Figure 2g) and it was found that they were highly consistent. Combining the above results, we believed that the Cu atom was directly linked to the nitrogen atom and oxygen atom, with bond lengths of 1.94 and 1.98 Å, respectively. The proposed asymmetric coordination moiety of CuN_1O_1 SAs/GAs is shown in Figure 2h. This unsaturated asymmetric Cu—N_1O_1 coordination structure was preserved mainly due to the shock effect caused by the transient pulse current.

2.3. Electrocatalytic Performance of CuN_1O_1 SAs/GAs on CO_2RR

A typical three-electrode system (Figure S20, Supporting Information) was employed to evaluate the CO_2RR performance on CuN_1O_1 SAs/GAs. Linear sweep voltammetry (LSV) was carried out for acquiring polarization curves of CuN_1O_1 SAs/GAs and CuN_4 SAs/GAs in the CO_2 saturated 0.5 м $KHCO_3$ aqueous solution. CuN_1O_1 SAs/GAs showed a larger current density than that of CuN_4 SAs/GAs under the same operated potential (**Figure** 3a), mainly due to different coordination moieties. Figure 3b exhibits the optimal FEs of CuN_1O_1 SAs/GAs electrode is 93.7% at −0.9 V, which is much higher than the CuN_4 SAs/GAs (75.5%). Besides, the current density of $HCOO^-$ production from CO_2RR is about −18 mA cm^{-2} at this FE (−0.9 V), as shown in Figure 3c. The current density of CuN_4 SAs/GAs is only −5.2 mA cm^{-2} at the same potential, which is weaker than that of CuN_1O_1 SAs/GAs. In the tested range (from −0.4 to −1.1 V), CuN_1O_1 SAs/GAs performed comprehensively better than CuN_4 SAs/GAs in catalytic properties, suggesting that the coordination structure of Cu—N_1O_1 is more suitable for the electrochemical production of $HCOO^-$ from CO_2RR, as an outstanding catalyst. The Tafel plots (J_{HCOO^-} vs overpotentials) were obtained at low current densities, and the electrochemical reaction was limited by electrochemical kinetics predominantly.[46,47] The Tafel slope of CuN_1O_1 SAs/GAs was lower than that of CuN_4 SAs/GAs, indicating that CuN_1O_1 SAs/GAs have faster electron dynamics and a faster electron transfer rate in the CO_2RR process (Figure S21, Supporting Information). Furthermore, the FE of CuN_1O_1 SAs/GAs for $HCOO^-$ could be kept >88% at the operated potential from −0.7 to −0.9 V versus RHE (Figure 3d), exhibiting excellent selectivity for $HCOO^-$ generation from CO_2RR, and this result is better than CuN_4 SAs/GAs under the same conditions (Figure S22, Supporting Information). The FEs of all products on CuN_1O_1 SAs/GAs in the whole potential interval are shown in Table S3 (Supporting Information). Moreover, CuN_1O_1 SAs/GAs surpassed the other listed catalysts on CO_2RR-to-formate recently reported (Figure S23 and Table S4, Supporting Information).

The long-term stability should not be neglected due to metal dissolution for CO_2RR.[48–50] Figure 3e presents the CuN_1O_1 SAs/GAs electrode maintaining over 86% FE with a stable current density (−19 mA cm^{-2}) for $HCOO^-$ production during 10 h stability measurement at −0.9 V versus RHE. The sample was subjected to structural analysis again after the stability test of electrocatalytic CO_2RR. As shown in Figure S24 (Supporting Information), according to the results of Cu K-edge XANES and EXAFS, the coordination structure of CuN_1O_1 SAs/GAs was not changed essentially after this test, manifesting that CuN_1O_1 SAs/GAs has excellent stability in the production of formic acid from CO_2. Additionally, CuN_1O_1 SAs/GAs maintained their characteristics as single atom catalysts without agglomeration after the stability test (Figure S25, Supporting Information). Therefore, these impressive performances of CuN_1O_1 SAs/GAs in terms of high activity, selectivity, and stability exhibit that it is competent for the practical electrode application in the electrocatalytic CO_2RR for formic acid production.

A flow cell with the gas diffusion electrodes (GDEs) was prepared (Figure 3f; Figure S26, Supporting Information) for investigating CO_2RR performance under the industrial current of CuN_1O_1 SAs/GAs. Figure 3g shows the LSV curves of CuN_1O_1 SAs/GAs and CuN_4 SAs/GAs in 0.5 м $KHCO_3$ solution, the current density of CuN_1O_1 SAs/GAs is much lower than CuN_4 SAs/GAs under the same conditions. The maximum of FE_{HCOO^-} reached 92.5% at −0.9 V versus RHE for CuN_1O_1 SAs/GAs, which is much higher than the FE_{HCOO^-} of CuN_4 SAs/GAs (50%), as shown in Figure 3h. The corresponding current density of $HCOO^-$ was decreased gradually with the increase of operated potentials (Figure S27, Supporting Information). The comparison of CO_2RR performance (flow cell) between CuN_1O_1 SAs/GAs and other catalysts reported in the literature is presented in Table S5 (Supporting Information). Moreover, the stability tests

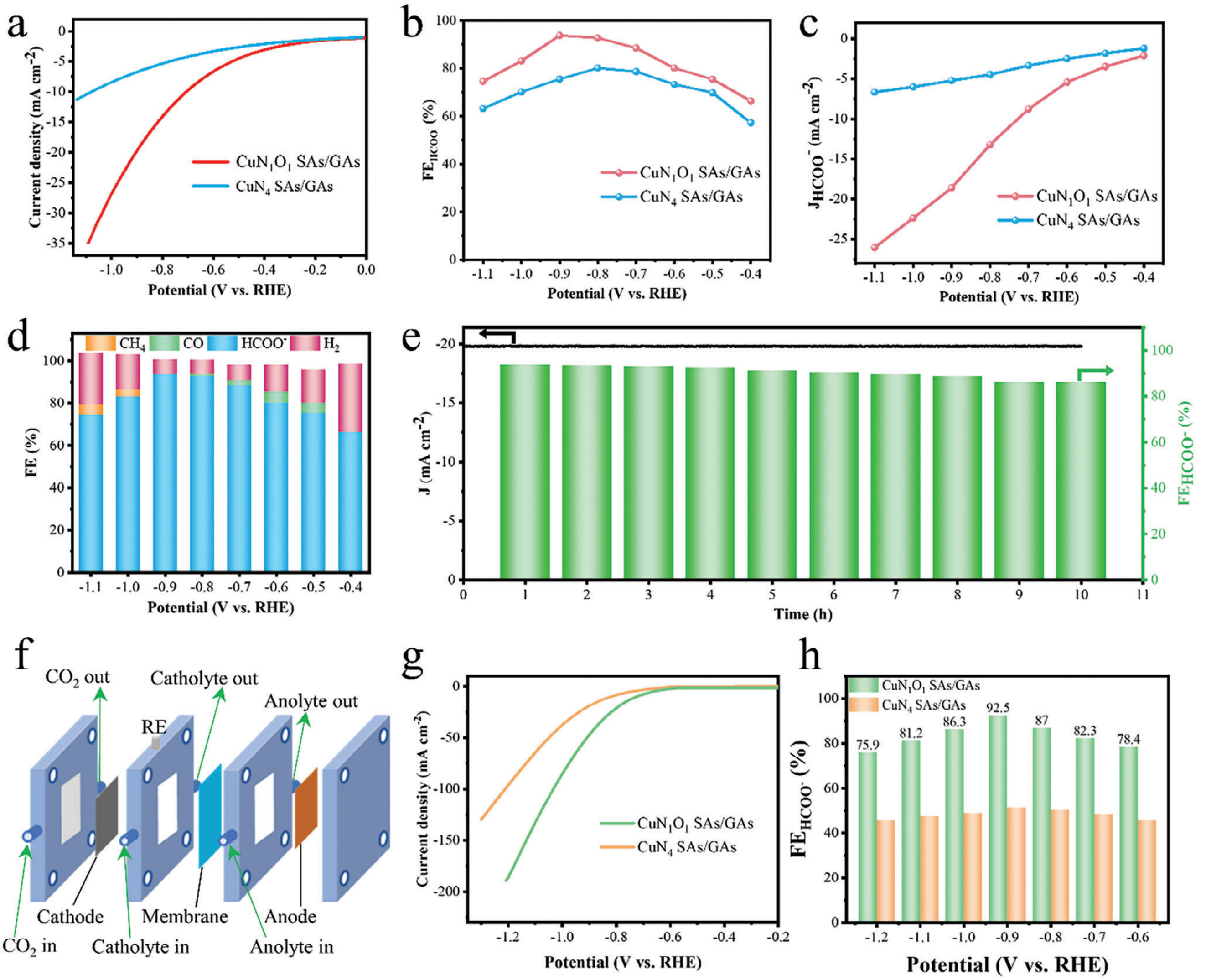

Figure 3. CO_2RR performance of CuN_1O_1 SAs/GAs. a) LSV curves of CuN_1O_1 SAs/GAs and CuN_4 SAs/GAs tested in CO_2 saturated electrolyte (0.5 м $KHCO_3$). b) Faradaic efficiency of $HCOO^-$ production measured by gas chromatography. c) Current densities of $HCOO^-$ production at different potentials. d) The FEs of diverse products for CuN_1O_1 SAs/GAs at different potentials. The total FEs are not 100% because of systems errors and the double layer current. e) Long-term stability test of CuN_1O_1 SAs/GAs at −0.9 V versus RHE. f) The structure diagram of the flow cell. g) LSV curves of CuN_1O_1 SAs/GAs and CuN_4 SAs/GAs. h) Faradaic efficiency of $HCOO^-$ production.

indicated that the degradation of FE_{HCOO^-} and operated potential were almost negligible at −50 mA cm^{-2} for CuN_1O_1 SAs/GAs (Figure S28, Supporting Information).

2.4. In Situ XAFS and ATR-FTIR Measurements of CuN_1O_1 SAs/GAs

To further study the structural transition characteristics of dispersed Cu sites on CuN_1O_1 SAs/GAs under electrocatalytic conditions,[51–53] a Cu K-edge XAFS measurement based on potential-dependent was performed (Figure S29, Supporting Information). **Figure** 4a presents the in situ Cu K-edge XANES spectra of CuN_1O_1 SAs/GAs during the CO_2RR process. The energy of the absorption position decreases gradually with the operated potential decreases from 0 to −0.9 V (inset of Figure 4a), and the white line peak intensity becomes lower, implying that the valence state of Cu in CuN_1O_1 SAs/GAs was changed during the CO_2RR process.[54,55] Figure 4b displays the first-derivative XANES curves of CuN_1O_1 SAs/GAs at different potentials and the references (Cu foil and CuO), the typical peak position was marked for identifying the various valence states of Cu. As shown in Figure 4c, the initial valence state of Cu in CuN_1O_1 SAs/GAs is 1.93, which is very close to the valence state of Cu in CuO (+2). When the operating potential was at the onset site, the valence state of Cu in CuN_1O_1 SAs/GAs decreased to 1.85, then to 1.79 at −0.6 V and 1.65 at −0.9 V. Additionally, the FT-EXAFS curves of CuN_1O_1 SAs/GAs at different potentials are depicted in Figure 4d. The main FT peak position gradually shifts to the left when the operating potential decreases, which demonstrates

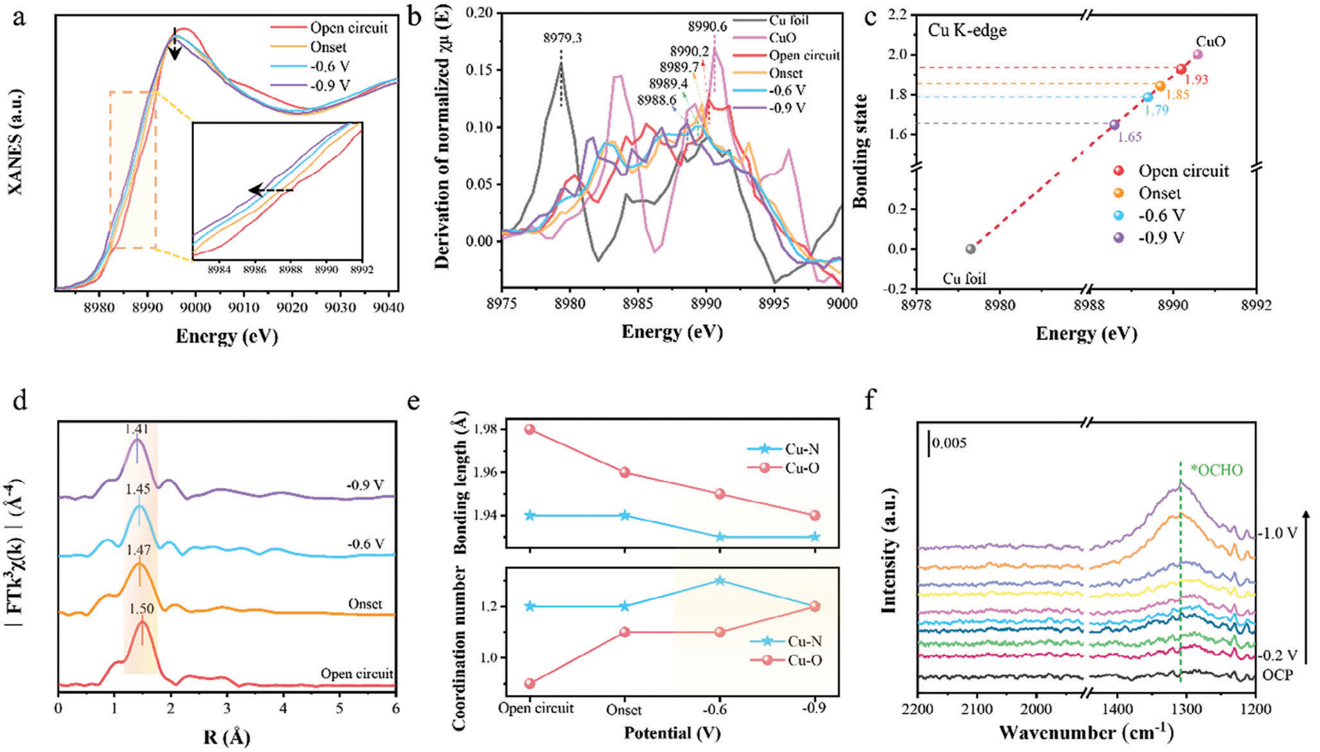

Figure 4. In situ XAFS and ATR-FTIR characterizations of CuN_1O_1 SAs/GAs. a) Cu K-edge XANES spectra of CuN_1O_1 SAs/GAs at different potentials during the CO_2RR process. The inset image is absorption edge evolution. b) First-derivative XANES curves of CuN_1O_1 SAs/GAs at different potentials and the references. c) The fitted average bonding states of Cu from the XANES spectra. d) k^3-weighted FT-EXAFS at open circuit, onset, −0.6 and −0.9 V versus RHE. The shaded region marked the changes in the peak positions of the first coordination shell. e) Changes of bond length and coordination number for the Cu—O and Cu—N coordination shells. f) In situ ATR-FTIR spectra results of CuN_1O_1 SAs/GAs.

that the average bond lengths of Cu—N/O are slightly contractive in the CO_2RR process (Figure 4e; Figures S30 and S31, Table S6, Supporting Information). As we can see, the in situ FT-EXAFS results tell us that the coordination bonds of the Cu—N/O are in a compression strain state in the reaction conditions, indicating that the low-valence pinched Cu—N_1O_1 coordination microenvironment provides the realistic active sites in the electrocatalytic CO_2RR to formic acid. The coordination number of the Cu—O bond was increased slightly due to an O atom in CO_2 absorbed by Cu atoms in the measurements, which is consistent with the theoretical calculation results as below. Meanwhile, although the asymmetric atomic interface is reconstructed to some extent, the original Cu—N/O coordination moiety is still maintained.

In situ attenuated total reflectance Fourier transform infrared spectroscopy (ATR-FTIR) was utilized to probe the intermediate (*OCHO) on CuN_1O_1 SAs/GAs with the operated potentials from −0.2 to −1.0 V versus RHE (Figure 4f; Figure S32, Supporting Information). No obvious *CO (for CO product) appeared at the range of 1900–2100 cm^{-1}. For CO_2 to $HCOO^-$ intermediates, *OCHO should be considered more efficient than *COOH during the CO_2RR process. Meanwhile, the definite *OCHO peak ≈1308 cm^{-1} on CuN_1O_1 SAs/GAs together with no visible *OCHO hydrogenation intermediates were probed in the tests, this peak gradually strengthened with the decrease of applied potentials.

2.5. Theoretical Study of CuN_1O_1 SAs/GAs on CO_2RR

To understand the excellent performance of CuN_1O_1 SAs/GAs in electrocatalytic CO_2 reduction to formic acid, the first-principles calculations were used to investigate the CO_2RR mechanism on the atomic interface of the catalyst.[56,57] The reaction pathways of CO, HCOOH, and CH_4 were fully considered and analyzed. According to the aforementioned experiments, we optimized two graphene-based structures: one with Cu, N, and O atoms (denoted as Cu—N_1O_1/C) and the other with Cu and O atoms (denoted as Cu—O_1C_1/C), see Figure S33 (Supporting Information). The Cu—N_1O_1/C exhibits a lower formation energy ΔE_f (7.01 eV) than the Cu—O_1C_1/C (7.92 eV), indicating the former is much more stable than the latter. After the Cu—N_1O_1 coordination moiety adsorbed O—C—O molecules, the charge rearranged (**Figure 5a**).

The evolution process of intermediates from CO_2 to HCOOH (pathway I) on the Cu—N_1O_1/C structure is described in Figure 5b, and another evolution procedure of intermediates from CO_2 to CO (pathway II) is displayed in Figure S34 (Supporting Information). Moreover, the Gibbs free energy plots of pathways I and II are exhibited in Figure 5c. For pathway I, the CO_2 was adsorbed to the Cu—N_1O_1/C structure with endothermic energy of 0.88 eV via the first electron addition, and then the adsorbed state of $^*OCO^-$ underwent an exothermic step of 2.17 eV to attract a proton and produce the adsorbed state of *OCHO.

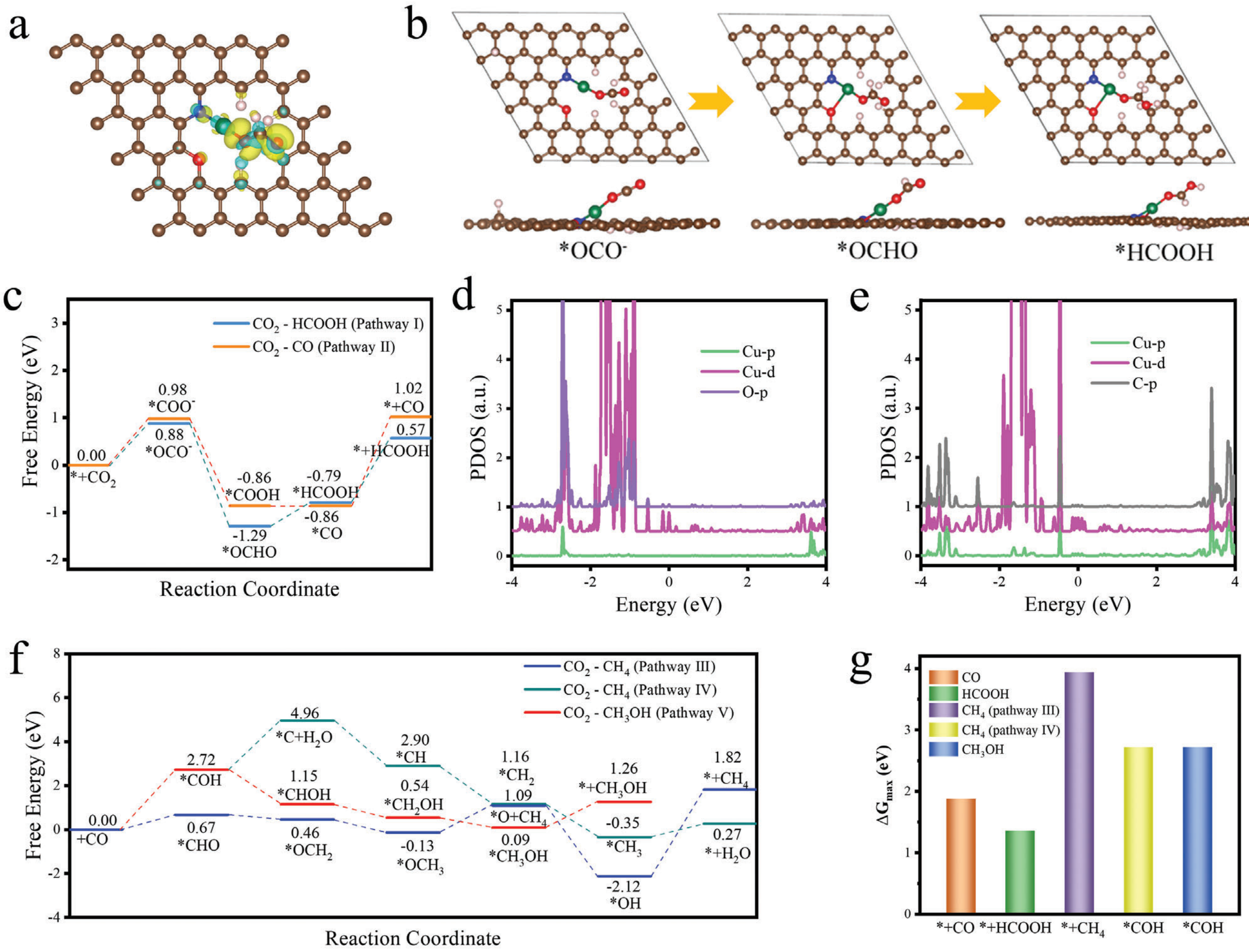

Figure 5. Theoretical CO_2RR activity of CuN_1O_1 SAs/GAs. a) The optimized structure of the adsorbed *OCHO and the differential charge density. b) The evolution process of intermediates from CO_2 to HCOOH (pathway I) on the Cu—N_1O_1/C structure. c) The Gibbs free energy diagrams of pathways I and II (from CO_2 to CO). d,e) The projected density of states of *OCHO and *COOH. f) The Gibbs free energy diagrams of pathways III, IV, and V (from CO_2 to CH_4 and CH_3OH). g) The maximum Gibbs free energy in all the steps of forming the pathways for CO, HCOOH, and CH_4/CH_3OH productions.

Subsequently, the *OCHO successively overcame two energy barriers of 0.50 and 1.36 eV to produce the product *HCOOH and released the HCOOH molecule. In contrast, the CO_2 was adsorbed to the Cu—N_1O_1/C structure with an endothermic energy of 0.98 eV for pathway II through the first electron addition. Then, the adsorbed $^*COO^-$ successively attracted two protons to produce the intermediate *COOH and the final produce *CO via an exothermic step of 1.84 eV and a step with no energy barrier, respectively. Finally, the adsorbed species *CO overcame one energy barrier of 1.88 eV to release the CO molecule. The lower energy barrier of the adsorbed $^*OCO^-$ indicated that CO_2 is more favored energetically to form the adsorbed $^*OCO^-$ on the Cu—N_1O_1/C. Compared with the projected density of states (PDOS) of *OCHO (Figure 5d) and *COOH (Figure 5e), *OCHO has a large number of charge overlaps (O_p and Cu_d orbitals) at −2 – 0 eV, while *COOH has only a small number of charge overlaps (C_p and Cu_d orbitals) at −2 – 0 eV. More electronic interactions indicated that the binding between *OCHO and Cu—N_1O_1 is more stable. As a whole, the potential limiting steps were shown to be the desorption of formate and CO in pathways I and II, respectively. The lower energy barrier in the desorption of formate indicated that the CO_2 is favorable energetically to produce the formate rather than CO on the Cu—N_1O_1/C surface.

Two main reduction pathways of CO_2 were considered:

I) For formate production:

$$* + CO_2 + e^- \rightarrow *OCO^- \tag{1}$$

$$* \ OCO^- + H^+ \rightarrow * \ COHO \tag{2}$$

$$*COHO + \left(H^+ + e^-\right) \rightarrow *HCOOH \tag{3}$$

$$*HCOOH \rightarrow * + HCOOH \tag{4}$$

II) For CO production:

$$* + CO_2 + e^- \rightarrow *COO^- \tag{5}$$

$$*COO^{-} + H^{+} \rightarrow *COOH \tag{6}$$

$$*COOH + \left(H^{+} + e^{-}\right) \rightarrow *CO + H_2O \tag{7}$$

$$*CO \rightarrow * + CO \tag{8}$$

CH_4 and CH_3OH products performed similar pathways from CO_2RR before the $^*CO$ intermediate formed.[58,59] Figure 5f describes the Gibbs free energy diagram for the reduction pathways of $^*CO$ and Figure S35 (Supporting Information) shows the corresponding intermediates and final products in the pathways. There exist two pathways for the transition from $^*CO$ to CH_4 and one pathway for the transition from $^*CO$ to CH_3OH: (III) $^*CO \rightarrow {}^*CHO \rightarrow {}^*OCH_2 \rightarrow {}^*OCH_3 \rightarrow {}^*O + CH_4$; (IV) $^*CO \rightarrow {}^*COH \rightarrow {}^*C \rightarrow {}^*CH \rightarrow {}^*CH_2 \rightarrow {}^*CH_3 \rightarrow CH_4$; (V) $^*CO \rightarrow {}^*COH \rightarrow {}^*CHOH \rightarrow {}^*CH_2OH \rightarrow {}^*CH_3OH \rightarrow CH_3OH$. The potential limiting steps for pathways IV and V are $^*CO \rightarrow {}^*COH$ with an energy barrier of 2.72 eV, while the limiting step for pathway III is $^*OCH_3 \rightarrow {}^*O + CH_4$ with an energy barrier of 1.21 eV. This indicated that the adsorbed CO is energetically favorable to produce CH_4 through pathway III. Comparing the maximum Gibbs free energy in all the steps of forming the pathways (Figure 5g), the maximum free energy change (1.22 eV) in the methane pathway III is the smallest among those in all pathways. However, the intermediate $^*O$ needs to overcome a high energy barrier of 3.94 eV to recover the catalyst surface, indicating that it is difficult to produce the amount of methane. In contrast, the maximum free energy change (1.36 eV) in the formic acid is the secondary lowest, indicating that formic acid is the easiest to produce, which is consistent with the results of the aforementioned experiments.

2.6. Synthesis and Structural Characterization of MN_1O_1 SAs/GAs (M = Mn, Fe, Co, and Ni)

The other metal elements (M = Mn, Fe, Co, and Ni) were easily generalized by the synthetic strategy in this study, simply requiring the change of copper nitrate to other metal nitrates. **Figures** 6a–t and S36 (Supporting Information) provide the HADDF-STEM images, the intensity profiles, the corresponding 3D intensity images, the distances of two metal atoms, and FT-EXAFS curves of MN_1O_1 SAs/GAs (the XANES results of MN_1O_1 SAs/GAs are shown in Figure S37 (Supporting Information), which clearly suggest the atomic dispersion feature of the metal species. Quantitative EXAFS fittings and the XANES paths are also carried out (Figures S38 and S39 and Table S7, Supporting Information), indicating that these MN_1O_1 SAs/GAs were typically twofold coordinated by 1 N atom and 1 O atom, just the same as the CuN_1O_1 SAs/GAs. The extended studies clearly demonstrate the generality of the strategy to construct isolated unsymmetrical active sites at the atomic scale.

3. Conclusion

In summary, for the first time, CuN_1O_1 SAs/GAs for CO_2RR including unsymmetrical Cu—N_1O_1 moieties dispersed on GAs were developed through a pulsed discharge approach. Originating from the sensible configuration of the active moieties, the CuN_1O_1 SAs/GAs sample performed optimal CO_2RR activity. The experimental investigations and theoretical calculations manifested that the improved electrocatalytic performance was constructed from the optimized atomic coordination structure and density of states feature of the concordantly unsaturated Cu—N_1O_1 moieties. The suggested scheme of coordinate structure tuning for SACs would facilitate the evolution of the novel catalysts for CO_2RR, including other electrochemical catalytic reactions for renewable energy developments, such as oxygen reduction reaction, hydrogen evolution reaction, and so on.

4. Experimental Section

Preparation of CuN_1O_1 SAs/GAs: In a typical synthesis, graphene oxide was fabricated by an improved Hummers method. The single-layer GO was diluted with deionized water (GO: $H_2O = 2$ mg g^{-1}), and fully stirred. The uniform GO aqueous dispersion was loaded into a hydrothermal reactor and heated at 180 °C for 6 h, the graphene hydrogel (GH) gradually formed. The GH was soaked in $Cu(NO_3)_2$ solution for 2 h, and then it was frozen quickly by liquid nitrogen. Afterward, GA loaded with copper nitrate ($Cu(NO_3)_2{\bullet}xH_2O/GA$) gradually formed through freeze drying. Then, $Cu(NO_3)_2{\bullet}xH_2O/GA$ was placed into the discharge tube for the pulsed current pulse treatment. Then the discharge tube was fixed to the pulsed discharge circuit. The charging voltage was set to be 8 kV. Once triggered, the intense current passes through the discharge tube and GA. The total period of discharge is ≈700 µs and the peak value of the current passing through GA is ≈60 kA. The discharge is repeated 8 times before recovery of the sample for the complete formation of single atoms onto GA. The characterizations of CuN_1O_1 SAs/GAs and other samples were depicted in the Note S2 (Supporting Information).

Electrochemical Measurements for CO_2RR: The electrochemical tests were carried out using a CHI Electrochemical Station (Model 760E) with a conventional three-electrode cell. Herein, an as-prepared electrode is a working electrode (WE), a pure platinum wire is used for a counter electrode (CE), and the reference electrode (RE) is Ag/AgCl in 0.5 M $KHCO_3$ solution. A Nafion membrane was placed between the anodic and cathodic chambers of the three-electrode cell. The catalysts inks obtained by a blend of catalysts (5 mg), isopropanol (0.75 mL), water (0.24 mL), and 5% Nafion solution (0.01 mL), subjected to ultrasound for 4 h. The catalysts ink (≈0.1 mL) was deposited onto carbon paper, and then dried in the air. The 0.5 M $KHCO_3$ aqueous solution (pH 7.3) was washed by Argon (0.5 h) before the measurement. In addition, the LSV curves would be recorded at 10 mV s^{-1} in the constant CO_2. Finally, all potentials were achieved to convert the RHE based on the Nernst equation ($E_{RHE} = E_{Ag/AgCl} + 0.0591 \times pH + 0.197$ V). The FE of the product in the CO_2RR test was calculated by: $FE = eF \times n/Q = eF \times n/(I \times t \times 100\%)$, where e is the amount of electrons transferred, F is the Faraday constant, n is the number of product, Q is the charge, I is current, and t is the running time. The potential was iR-corrected. In flow cell measurement, the cathode electrode was prepared by a gas diffusion layer (GDL) deposited by catalyst inks. The counter electrode was used by IrO_2, which was obtained by IrO_2 catalyst inks loaded on a GDL (0.7 mg cm^{-2}). The IrO_2 catalyst inks were ultrasonically mixed with commercial IrO_2 powder (5 mg), isopropanol (0.75 mL), water (0.24 mL), and 5% Nafion solution (0.01 mL) for 4 h. CO_2 gas flowed behind the GDL cathode at the rate of 30 standard cubic centimeters per minute.

XAFS Measurements: The XAFS spectra (Cu, Mn, Fe, Co, and Ni K-edge) were obtained at 1W1B station in Beijing Synchrotron Radiation Facility. All the XAFS data were obtained in the fluorescence excitation mode. The samples were prepared as disks with the diameter and thickness were 13 and 1 mm, respectively. The XAFS data analysis was exhibited in Note S3 (Supporting Information). The in situ synchrotron radiation XAFS measurements and the theoretical XANES simulations were displayed in Notes S4 and S5 (Supporting Information).

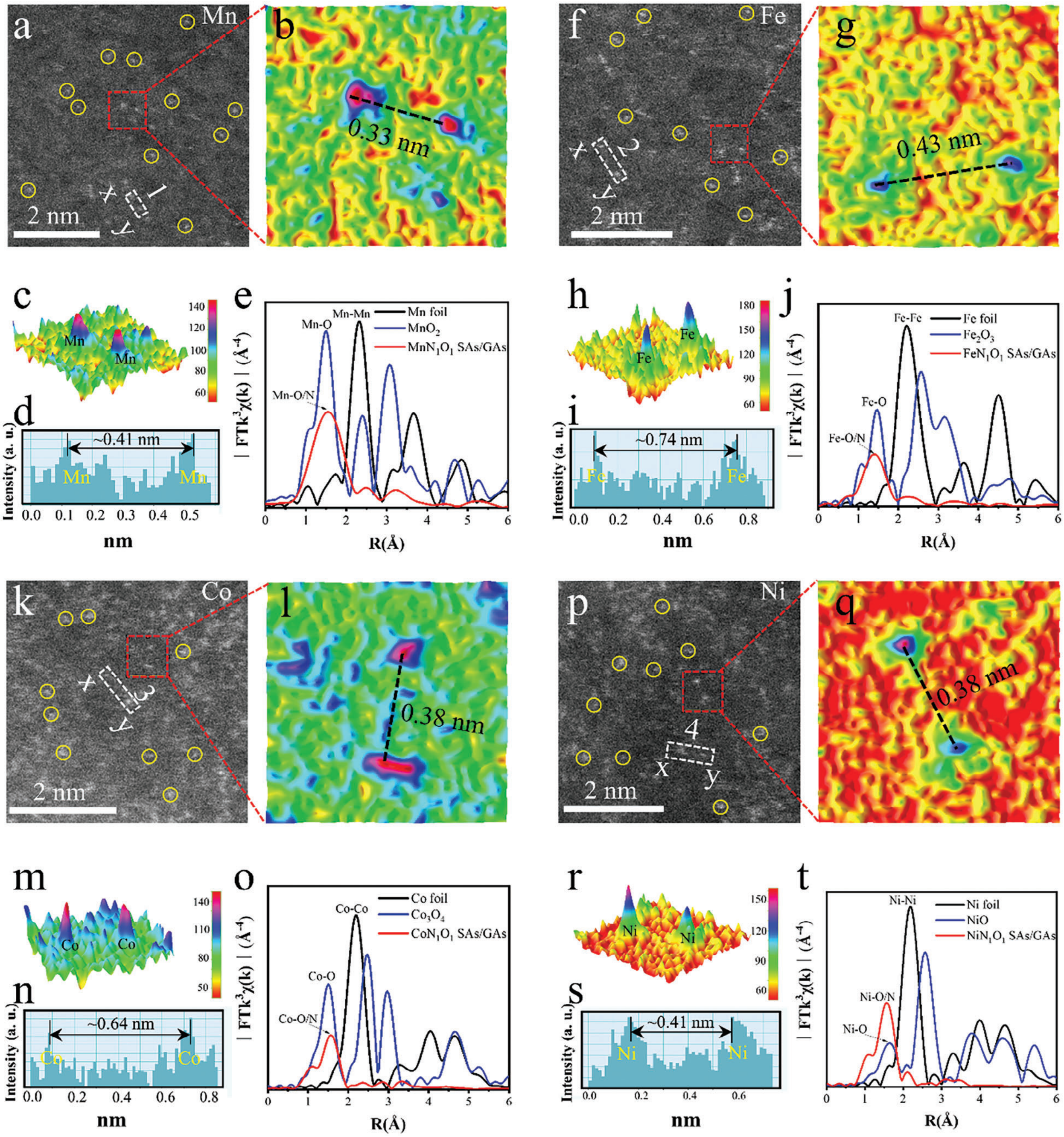

Figure 6. HAADF-STEM and FT-EXAFS characterizations of MN$_1$O$_1$ SAs/GAs (M = Mn, Fe, Co, Ni). The HAADF-STEM image (a), The intensity profile (b) of the yellow box in (a), The corresponding 3D intensity (c) of (b), The length of two Mn atoms (d) of (a), FT-EXAFS spectra (e) for MnN$_1$O$_1$ SAs/GAs. The HAADF-STEM image (f), The intensity profile (g) of the yellow box in (f), The corresponding 3D intensity (h) of (g), The length of two Fe atoms (i) of (f), FT-EXAFS spectra (j) for FeN$_1$O$_1$ SAs/GAs. The HAADF-STEM image (k), The intensity profile (l) of the yellow box in (k), The corresponding 3D intensity (m) of (l), The length of two Co atoms (n) of (k), FT-EXAFS spectra (o) for CoN$_1$O$_1$ SAs/GAs. The HAADF-STEM image (p), The intensity profile (q) of the yellow box in (p), The corresponding 3D intensity (r) of (p), The length of two Ni atoms (s) of (p), FT-EXAFS spectra (t) for NiN$_1$O$_1$ SAs/GAs.

In Situ ATR-FTIR: In situ ATR-FTIR was performed on a Thermo-Fisher Nicolet iS20 spectrometer. The electrochemical measurement was carried out in a three-electrode electrochemical cell. The 0.5 м $KHCO_3$ solution (pH 7.3) was utilized as the electrolyte. In this test, the spectral resolution was 4 cm^{-1}, and the spectrum recorded at open circuit potential (OCP) was used as a comparison, the test recorded range was from 0 to −1.0 V versus RHE.

The Detail of DFT Calculations: The graphene-based structure including the Cu, O, and N atoms was built with a vacuum space of 20 Å along the *z*-direction (see Figure 5a). Then the intermediates for CO, HCOOH, CH_4, and CH_3OH products were adsorbed on the SACs. The Vienna Ab Initio Simulation Package (VASP) was used to execute the density functional theory (DFT) calculations for all structures. The spin-polarized generalized gradient approximation (GGA) was employed using the Perdew–Burke–Ernzerhof (PBE) formulation to calculate the exchange and correlation energies. The projector-augmented wave (PAW) method was chosen to describe the valence-core interactions. The method takes 4, 5, 11, 6, and 1 valence electrons into account using a plane wave basis site with a kinetic energy cutoff of 700 eV for C, N, Cu, O, and H, respectively. K-points sampling of 2 × 2 × 1 was used for all structures. All the atoms were relaxed during structural optimization. The energy threshold was set to 1×10^{-5} eV and the force on each atom was set to 0.01 eV $Å^{-1}$. The spin polarization was considered and the DFT-D3 method of Grimme was employed. The vibrational frequency of the structures was achieved by the numerical finite displacement method, which was crucial for zero-point energy (ZPE) correction. For adsorbate on a solid surface, the ZPE-corrected energy is a good approximation to the Gibbs free energy.

The formation energies of the graphene-based structures with Cu, N, and O atoms were estimated by the following formula:

$$\Delta E_f = E_{sys} - n_C \times \mu_C - n_N \times \mu_N - n_H \times \mu_H - n_O \times \mu_O - \mu_{Cu} \tag{9}$$

where E_{sys} is the total energy of each system; n_C, n_N, n_H, and n_O denote the number of C, N, H, and O atoms in the system; μ_C, μN, μ_H, μ_O, and μ_{Cu} are the chemical potentials of C, N, H, O, and Cu atoms, denoting the energy of per C, N, H, O, and Cu in graphite, N_2, H_2, O_2 gas, and Cu bulk.

Supporting Information

Supporting Information is available from the Wiley Online Library or from the author.

Acknowledgements

This work was supported by the National Natural Science Foundation of China (Grant nos. 12372332 and 12002048), the Beijing Natural Science Foundation (Grant No. 2212018), the Beijing Institute of Technology Research Fund Program for Young Scholars (Grant no. 2022CX01011 and XSQD-202002004), and the Beijing Institute of Technology Research and Innovation Promoting Project (Grant No. 2022YCXZ003).

Conflict of Interest

The authors declare no conflict of interest.

Data Availability Statement

The data that support the findings of this study are available from the corresponding author upon reasonable request.

Keywords

CO_2 reduction, formate, pulsed discharge, single atom catalysts

Received: October 13, 2023
Revised: December 12, 2023
Published online: January 3, 2024

---

[1] V. M. Luna, C. Anacker, N. S. Burghardt, H. Khandaker, V. Andreu, A. Millette, P. Leary, R. Ravenelle, J. C. Jimenez, A. Mastrodonato, C. A. Denny, A. A. Fenton, H. E. Scharfman, R. Hen, *Science* **2019**, *364*, 578.
[2] S. Chu, A. Majumdar, *Nature* **2012**, *488*, 294.
[3] S. Gao, Y. Lin, X. Jiao, Y. Sun, Q. Luo, W. Zhang, D. Li, J. Yang, Y. Xie, *Nature* **2016**, *529*, 68.
[4] B. Wei, Y. Xiong, Z. Zhang, J. Hao, L. Li, W. Shi, *Appl. Catal., B* **2021**, *283*, 119646.
[5] Y. Liu, T. Wu, H. Cheng, J. Wu, X. Guo, H. J. Fan, *Nano Res.* **2023**, *16*, 10803.
[6] F. Lei, W. Liu, Y. Sun, J. Xu, K. Liu, L. Liang, T. Yao, B. Pan, S. Wei, Y. Xie, *Nat. Commun.* **2016**, *7*, 12697.
[7] Y. Qiao, W. Lai, K. Huang, T. Yu, Q. Wang, L. Gao, Z. Yang, Z. Ma, T. Sun, M. Liu, C. Lian, H. Huang, *ACS Catal.* **2022**, *12*, 2357.
[8] W. Luo, W. Xie, M. Li, J. Zhang, A. Züttel, *J. Mater. Chem. A.* **2019**, *7*, 4505.
[9] N. Zouaoui, B. D. Ossonon, M. Fan, D. Mayilukila, S. Garbarino, G. De Silveira, G. A. Botton, D. Guay, A. C. Tavares, *J. Mater. Chem. A.* **2019**, *7*, 11272.
[10] B. Jiang, X.-G. Zhang, K. Jiang, D.-Y. Wu, W.-B. Cai, *J. Am. Chem. Soc.* **2018**, *140*, 2880.
[11] H. Shen, H. Jin, H. Li, H. Wang, J. Duan, Y. Jiao, S.-Z. Qiao, *Nat. Commun.* **2023**, *14*, 2843.
[12] J. H. Koh, D. H. Won, T. Eom, N.-K. Kim, K. D. Jung, H. Kim, Y. J. Hwang, B. K. Min, *ACS Catal.* **2017**, *7*, 5071.
[13] W. Liu, L. Ding, M. Liu, X. Wang, Z. Zhang, T.-W. Jiang, S. Huo, W.-B. Cai, *Nano Res.* **2023**, *16*, 10822.
[14] S. Yang, M. Jiang, W. Zhang, Y. Hu, J. Liang, Y. Wang, Z. Tie, Z. Jin, *Adv. Funct. Mater.* **2023**, *33*, 2301984.
[15] Z. Wu, H. Wu, W. Cai, Z. Wen, B. Jia, L. Wang, W. Jin, T. Ma, *Angew. Chem., Int. Ed.* **2021**, *60*, 12554.
[16] W. Liu, H. Li, P. Ou, J. Mao, L. Han, J. Song, J. Luo, H. L. Xin, *Nano Res.* **2023**, *16*, 8729.
[17] T. Zheng, C. Liu, C. Guo, M. Zhang, X. Li, Q. Jiang, W. Xue, H. Li, A. Li, C.-W. Pao, J. Xiao, C. Xia, J. Zeng, *Nat. Nanotechnol.* **2021**, *16*, 1386.
[18] H. Xu, D. Rebollar, H. He, L. Chong, Y. Liu, C. Liu, C.-J. Sun, T. Li, J. V. Muntean, R. E. Winans, D.-J. Liu, T. Xu, *Nat. Energy* **2020**, *5*, 623.
[19] L. Li, I. M. Hasan, Farwa, R. He, L. Peng, N. Xu, N. K. Niazi, J. N. Zhang, J. Qiao, *Nano Re. Energy* **2022**, *1*, e9120015.
[20] M. T. Greiner, T. E. Jones, S. Beeg, L. Zwiener, M. Scherzer, F. Girgsdies, S. Piccinin, M. Armbrüster, A. Knop-Gericke, R. Schlögl, *Nat. Chem.* **2018**, *10*, 1008.
[21] Y. Cheng, H. Wang, H. Song, K. Zhang, G. I. N. Waterhouse, J. Chang, Z. Tang, S. Lu, *Nano Res. Energy* **2023**, *2*, e9120082.
[22] N. Han, P. Ding, L. He, Y. Li, Y. Li, *Adv. Energy Mater.* **2020**, *10*, 1902338.
[23] J. Shen, D. Wang, *Nano Research Energy* **2024**, *3*, e9120096.
[24] X. Ye, C. Yang, X. Pan, J. Ma, Y. Zhang, Y. Ren, X. Liu, L. Li, Y. Huang, *J. Am. Chem. Soc.* **2020**, *142*, 19001.
[25] J. Gu, C.-S. Hsu, L. Bai, H. M. Chen, X. Hu, *Science* **2019**, *364*, 1091.
[26] A. Wang, J. Li, T. Zhang, *Nat. Rev. Chem.* **2018**, *2*, 65.
[27] H. Zhang, P. An, W. Zhou, B. Y. Guan, P. Zhang, J. Dong, X. W. Lou, *Sci. Adv.* **2018**, *4*, eaao6657.
[28] D. Zhong, D. Zhang, W. Chen, J. He, C. Ren, X. Zhang, N. Kong, W. Tao, M. Zhou, *Sci. Adv.* **2021**, *7*, eabl4915.
[29] T. Gan, D. Wang, *Nano Res.* **2023**, https://doi.org/10.1007/s12274-023-5700-4.
[30] G. He, M. Yan, H. Gong, H. Fei, S. Wang, *Int. J. Extrem. Manuf.* **2022**, *4*, 032003.
[31] Y. Yao, Z. Huang, P. Xie, L. Wu, L. Ma, T. Li, Z. Pang, M. Jiao, Z. Liang, J. Gao, Y. He, D. J. Kline, M. R. Zachariah, C. Wang, J. Lu, T. Wu, T. Li, C. Wang, R. Shahbazian-Yassar, L. Hu, *Nat. Nanotechnol.* **2019**, *14*, 851.
[32] Y. Peng, J. Cao, Y. Sha, W. Yang, L. Li, Z. Liu, *Light Sci. Appl.* **2021**, *10*, 168.

[33] J. Du, G. Wu, K. Liang, J. Yang, Y. Zhang, Y. Lin, X. Zheng, Z.-Q. Yu, Y. Wu, X. Hong, *Small* **2021**, *17*, 2007264.
[34] C. Li, R. Han, J. Bai, Y. Cao, W. Yuan, J. Wu, P. Li, X. Chen, *Carbon* **2023**, *213*, 118296.
[35] J.-Y. Song, C. Kim, M. Kim, K. M. Cho, I. Gereige, W.-B. Jung, H. Jeong, H.-T. Jung, *Sci. Adv.* **2021**, *7*, eabk2984.
[36] H. Xie, X. Xie, G. Hu, V. Prabhakaran, S. Saha, L. Gonzalez-Lopez, A. H. Phakatkar, M. Hong, M. Wu, R. Shahbazian-Yassar, V. Ramani, M. I. Al-Sheikhly, D.-E. Jiang, Y. Shao, L. Hu, *Nat. Energy* **2022**, *7*, 281.
[37] Z. Huang, Y. Yao, Z. Pang, Y. Yuan, T. Li, K. He, X. Hu, J. Cheng, W. Yao, Y. Liu, A. Nie, S. Sharifi-Asl, M. Cheng, B. Song, K. Amine, J. Lu, T. Li, L. Hu, R. Shahbazian-Yassar, *Nat. Commun.* **2020**, *11*, 6373.
[38] D. Jiang, Y. Yao, T. Li, G. Wan, X. I. Pereira-Hernández, Y. Lu, J. Tian, K. Khivantsev, M. H. Engelhard, C. Sun, C. E. García-Vargas, A. S. Hoffman, S. R. Bare, A. K. Datye, L. Hu, Y. Wang, *Angew. Chem., Int. Ed.* **2021**, *60*, 26054.
[39] X. Wang, Y. Wei, H. Zhou, Q. Liu, L. Zhu, *Ceram. Int.* **2021**, *47*, 21934.
[40] G. S. Sarkisov, A. Hamilton, V. I. Sotnikov, *Phys. Rev. E* **2018**, *98*, 053203.
[41] P. Chen, N. Zhang, S. Wang, T. Zhou, Y. Tong, C. Ao, W. Yan, L. Zhang, W. Chu, C. Wu, Y. Xie, *Proc. Natl. Acad. Sci. USA* **2019**, *116*, 6635.
[42] H. Shang, X. Zhou, J. Dong, A. Li, X. Zhao, Q. Liu, Y. Lin, J. Pei, Z. Li, Z. Jiang, D. Zhou, L. Zheng, Y. Wang, J. Zhou, Z. Yang, R. Cao, R. Sarangi, T. Sun, X. Yang, X. Zheng, W. Yan, Z. Zhuang, J. Li, W. Chen, D. Wang, J. Zhang, Y. Li, *Nat. Commun.* **2020**, *11*, 3049.
[43] Y. Cai, J. Fu, Y. Zhou, Y.-C. Chang, Q. Min, J.-J. Zhu, Y. Lin, W. Zhu, *Nat. Commun.* **2021**, *12*, 586.
[44] C. Tang, L. Chen, H. Li, L. Li, Y. Jiao, Y. Zheng, H. Xu, K. Davey, S.-Z. Qiao, *J. Am. Chem. Soc.* **2021**, *143*, 7819.
[45] H. Fei, J. Dong, Y. Feng, C. S. Allen, C. Wan, B. Volosskiy, M. Li, Z. Zhao, Y. Wang, H. Sun, P. An, W. Chen, Z. Guo, C. Lee, D. Chen, I. Shakir, M. Liu, T. Hu, Y. Li, A. I. Kirkland, X. Duan, Y. Huang, *Nat. Catal.* **2018**, *1*, 63.
[46] S. Liu, X. F. Lu, J. Xiao, X. Wang, X. W. Lou, *Angew. Chem., Int. Ed.* **2019**, *58*, 13828.
[47] S. Lee, H. Ju, R. Machunda, S. Uhm, J. K. Lee, H. J. Lee, J. Lee, *J. Mater. Chem. A.* **2015**, *3*, 3029.
[48] S. Liu, J. Xiao, X. F. Lu, J. Wang, X. Wang, X. W. Lou, *Angew. Chem., Int. Ed.* **2019**, *58*, 8499.
[49] L. Fan, C. Xia, P. Zhu, Y. Lu, H. Wang, *Nat. Commun.* **2020**, *11*, 3633.
[50] M. A. A. Mahbub, J. R. C. Junqueira, X. Wang, J. Zhang, S. Dieckhöfer, S. Seisel, D. Das, W. Schuhmann, *Adv. Funct. Mater.* **2023**, 2307752.
[51] Y. Deng, J. Zhao, S. Wang, R. Chen, J. Ding, H.-J. Tsai, W.-J. Zeng, S.-F. Hung, W. Xu, J. Wang, F. Jaouen, X. Li, Y. Huang, B. Liu, *J. Am. Chem. Soc.* **2023**, *145*, 7242.
[52] W. Cheng, H. Su, Q. Liu, *Acc. Chem. Res.* **2022**, *55*, 1949.
[53] B. Jia, L. Li, C. Xue, J. Kang, L.-M. Liu, T. Guo, Z. Wang, Q. Huang, S. Guo, *Adv. Mater.* **2023**, *35*, 2305587.
[54] Y.-T. Xu, M.-Y. Xie, H. Zhong, Y. Cao, *ACS Catal.* **2022**, *12*, 8698.
[55] T. Zhang, A. G. Walsh, J. Yu, P. Zhang, *Chem. Soc. Rev.* **2021**, *50*, 569.
[56] H. B. Yang, S.-F. Hung, S. Liu, K. Yuan, S. Miao, L. Zhang, X. Huang, H.-Y. Wang, W. Cai, R. Chen, J. Gao, X. Yang, W. Chen, Y. Huang, H. M. Chen, C. M. Li, T. Zhang, B. Liu, *Nat. Energy* **2018**, *3*, 140.
[57] Y. Fu, S. Jin, X.-Y. Zhu, *Nat. Rev. Chem.* **2021**, *5*, 838.
[58] L. Zhang, X.-X. Li, Z.-L. Lang, Y. Liu, J. Liu, L. Yuan, W.-Y. Lu, Y.-S. Xia, L.-Z. Dong, D.-Q. Yuan, Y.-Q. Lan, *J. Am. Chem. Soc.* **2021**, *143*, 3808.
[59] C. Li, Z. Liu, X. Zhou, L. Zhang, Z. Fu, Y. Wu, X. Lv, G. Zheng, H. Chen, *Energy Environ. Sci.* **2023**, *16*, 3885.